PHYSICAL REVIEW B VOLUME 59, NUMBER 8 15 FEBRUARY 1999-II

Holographic atomic images from surface and bulk W(110) photoelectron diffraction data

P. M. Len
Physics Department, University of California, Davis, California 95616
and Materials Sciences Division, Lawrence Berkeley National Laboratory, University of California, Berkeley, California 94720

J. D. Denlinger*
Department of Physics, University of Wisconsin, Milwaukee, Wisconsin 53211

E. Rotenberg* and S. D. Kevan
Department of Physics, University of Oregon, Eugene, Oregon 97403

B. P. Tonner
Department of Physics, University of Wisconsin, Milwaukee, Wisconsin 53211

Y. Chen and M. A. Van Hove
Materials Sciences Division, Lawrence Berkeley National Laboratory, University of California, Berkeley, California 94720

C. S. Fadley
Physics Department, University of California, Davis, California 95616
and Materials Sciences Division, Lawrence Berkeley National Laboratory, University of California, Berkeley, California 94720

(Received 6 March 1998)

Photoelectron diffraction data can, in principle, be regarded as enabling the experimental recording of electron diffraction phases (relative to a direct reference wave), as well as intensities, thus also permitting the holographic reconstruction of atomic positions. Such holographic photoelectron diffraction patterns have been measured for surface and bulk core-level-shifted W $4f$ photoemission from W(110), yielding a data set of unprecedented size and quality. To test the role of experimental uncertainties and of multiple-scattering effects, we have also performed corresponding theoretical calculations at the single- and multiple-scattering levels. The surface and bulk holograms so obtained have been analyzed so as to provide the first parallel comparison of the three-dimensional atomic images that can be directly obtained via the five principal reconstruction algorithms proposed to date. The advantages and disadvantages of each of these methods are discussed. The prospects and limitations of atomic photoelectron holography as an *ab initio* technique for determining local-surface structures are also explored. [S0163-1829(99)08207-7]

I. INTRODUCTION

Gabor originally proposed holography with electron beams as an experimental scheme to directly record the intensities and phases of diffraction patterns relative to a reference wave front.[1] Later, Szöke observed that far-field photoelectron and fluorescent x-ray diffraction patterns created by the interference between a direct unscattered wave front and wave fronts scattered by atoms neighboring the emitting atom are also holographic in nature.[2] As both diffraction intensities and phases can thus be determined experimentally, three-dimensional images of the superpositions of the atomic neighborhoods of each emitting site can then be directly obtained using various reconstruction algorithms,[3–8] as experimentally demonstrated by now in photoelectron diffraction,[9] Auger electron diffraction,[10] Kikuchi-electron backscattering,[11] low-energy electron diffraction,[12] and positron diffraction.[13] More recently, similar holographic imaging has been demonstrated experimentally in x-ray fluorescence as well.[14,15] Some of the notable successes of photoelectron holography to date involve the determination of the structures of adsorbate overlayers,[6(b),9(c),11(a),12(a)] and reconstructed surfaces.[6(d),9(e),11(b)] A significant advantage of photoelectron holography is in being able, via core-level binding-energy shifts, to study the local structure around each type of emitter separately, and we make use of that aspect here.

However, due to the nonideal nature of electron emission and scattering, atomic images obtained from all electron holograms suffer from aberrations, artifacts, and position shifts[16–18] relative to, e.g., the more accurate atomic images expected from x-ray holograms; this is due to the more ideal nature of the x-ray emission and scattering processes.[19] In this paper, we will compare the most often-used reconstruction algorithms for photoelectron holography that attempt to increase atomic image fidelity by in some way suppressing and/or directly accounting for the nonideal nature of electron-scattering processes. Preliminary theoretical comparisons have been made earlier between these different reconstruction algorithms,[20] but to our knowledge this paper represents the first such comprehensive comparison of these imaging methods as applied to a very large and high-quality experimental data set involving photoelectrons from both surface and bulk atoms, as distinguished via their core-level shifts on the W(110) surface.

The W(110) surface represents an excellent test system for photoelectron holography, as it has been studied previously by various surface-structure probes, including low-energy electron diffraction[21(a)–21(c)] (LEED) and both scanned-energy[21(d),21(e)] and scanned-angle[21(f)] photoelectron diffraction (PD). The surface is known to be unreconstructed, and to have a surface-layer-to-second-layer distance that is very little relaxed from the bulk distance, with LEED studies yielding no relaxation,[21(a),21(b)] or a 0.069-Å inward relaxation of the surface layer relative to the bulk distance.[21(c)] A similar analysis of scanned-energy PD data yields a 0.03-Å outward relaxation[21(d)] to a 0.2-Å outward relaxation,[21(e)] and a more recent analysis of full-hemisphere scanned-angle PD data yields a 0.10-Å outward relaxation.[21(f)] To a sufficient accuracy for modeling the photoelectron holograms for this surface, we can thus assume no interlayer relaxation. A further advantage of this surface for PD studies is that it exhibits a very large surface core-level shift of 320 meV relative to the bulk. Thus, the emission from both the outermost surface layer (an ''adsorbate'' layer in which backscattering and side scattering are dominant) and the underlying bulk layers [a three-dimensional (3D) lattice in which forward scattering is dominant] can be distinguished in a high-resolution spectrum, and the resulting holograms used to generate separate images of their near-neighbor atoms. Finally, studying W should provide a critical test of theory, in that this high-Z scatterer should lead to highly anisotropic atomic scattering and strong multiple-scattering effects.

II. EXPERIMENTAL DETERMINATION OF NORMALIZED HOLOGRAMS

Photoelectron diffraction data from clean W(110) were collected at undulator beamline 7.0 of the Advanced Light Source at the Lawrence Berkeley National Laboratory, using a hemispherical analyzer in the UltraESCA end station. The experimental geometry is shown in Fig. 1(a); the incidence direction, the outgoing photoelectron $\mathbf{k}$ vector, and the surface normal are coplanar in the plane of the figure. The W $4f$ photoelectron peak can be resolved into surface and bulk core-level shifted components, as shown in Fig. 1(b). For each energy and direction studied, the W $4f$ peak was resolved into surface and bulk emission components by integrating the areas under the higher and lower flanks of the photoemission surface and bulk W $4f$ peaks, respectively, as shown by the shaded areas in Fig. 1(b). Such photoelectron spectra were measured for kinetic energies of $E = 41-197\,\text{eV}$ (wave vectors $k = 3.3-7.2\,\text{Å}^{-1}$), and collected over a polar takeoff angle range of $14° \leqslant \theta \leqslant 90° \equiv$ normal emission. These data points were measured at wave vector intervals corresponding to $\delta k = 0.1\,\text{Å}^{-1}$, and angular intervals of $(\delta\theta, \delta\phi) = (3°, 3°/\cos\theta)$ corresponding to roughly equal solid-angle elements, making a total of 12 280 unique measurements in a symmetry-reduced $\frac{1}{4}$ of the total solid angle above the sample.

Figures 2(a) and 3(a) show cut away $\mathbf{k}$ space volume representations of the surface and bulk $I(\mathbf{k})$ data sets, respectively. The vertical scale is photoelectron wave vector, ranging from $k = 3.85$ to 7.45 Å^{-1} (kinetic energy is $E = 56$ to 211 eV), and the polar angles range from $40° \leqslant \theta \leqslant 90°$, as adjusted using an inner potential correction of $V_0 = 14\,\text{V}$ (Ref. 25) to yield electron wave vectors *and* directions beneath the surface of the sample. Thus, data was omitted for the lower polar angles that would lie below the lowest common polar angle of $\theta = 40°$ *after* the inner potential correction. Due to the strong atomic scattering of electrons (as compared, e.g., to fluorescent x-rays), the anisotropy of the raw $I(\mathbf{k})$ data, defined as $\Delta I/I_0 = (I_{\max} - I_{\min})/I_0$ and $\approx 30\%$ is easily discernible with this gray scale. This can be compared to raw $I(\mathbf{k})$ data for fluorescent x rays, which has anisotropies about two orders of magnitude less.[22]

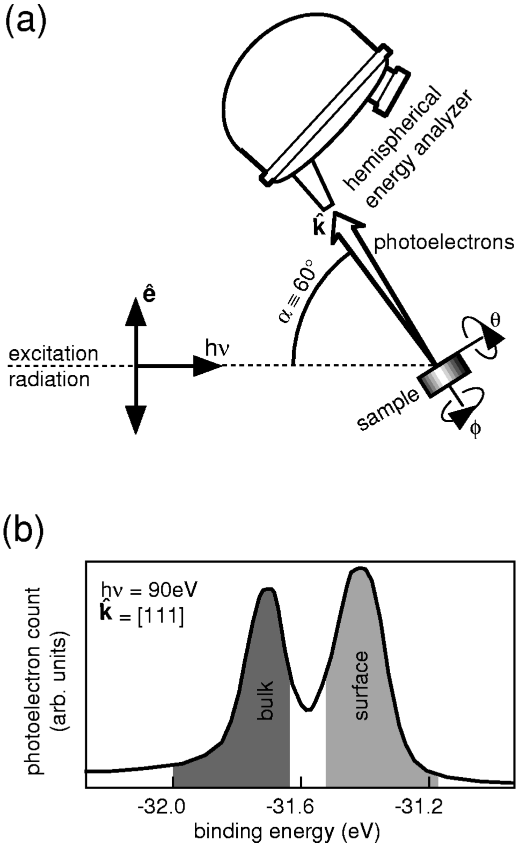

FIG. 1. (a) Experimental geometry, including the orientation of the sample (where $\hat{\mathbf{n}}$ is the surface normal) with respect to the horizontal polarization vector ($\hat{\mathbf{e}}$) of the incident excitation radiation $h\nu$, and the exit photoelectron direction $\mathbf{k}$. The angle between the incident photons and the emitted photoelectrons, as detected by a hemispherical analyzer, is fixed at 60°. The polar takeoff angle θ is varied by rotating the sample about an axis lying in the surface and in the plane containing $\hat{\mathbf{e}}$ and $\mathbf{k}$; the azimuthal angle ϕ is varied by rotating about $\hat{\mathbf{n}}$. (b) Typical W $4f_{7/2}$ x-ray photoelectron spectrum from W(110), indicating the surface and bulk core-level-shifted contributions used to generate the holographic $I(\mathbf{k})$ intensity data points of Figs. 2 and 3.

Before atomic images can be reconstructed from these $I(\mathbf{k})$ data sets, normalized holographic intensities were obtained via $\chi(\mathbf{k}) \equiv [I(\mathbf{k}) - I_0(\mathbf{k})]/\sqrt{I_0(\mathbf{k})}$, where $I_0(\mathbf{k})$ is the intensity that would be measured in the absence of atomic scattering (i.e., the intensity of the reference wave, including any modulations due to geometrical excitation or instrumental effects). Dividing by $I_0(\mathbf{k})$ in deriving $\chi(\mathbf{k})$ has also been done in some studies,[6(c),9(d),11(b)] but in practice, we find there is little difference in the final holographic images between this choice and dividing by $\sqrt{I_0(\mathbf{k})}$. In practice, this $I_0(\mathbf{k})$

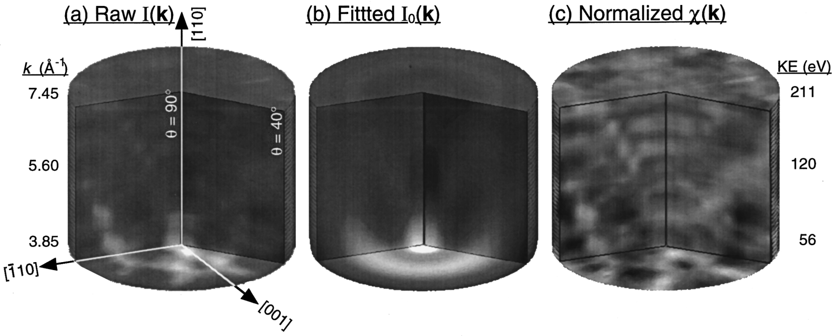

FIG. 2. **k**-space volume representations of the intensity data sets for surface W $4f_{7/2}$ emission. Wave vectors (vertical scale) and polar angles (horizontal scale) have here all been adjusted to be inside the surface, using an inner potential of $V_0 = 14\,\text{V}$. (a) Raw $I(\mathbf{k})$ data set. (b) $I_0(\mathbf{k})$ as determined by a least-squares fit in wave vector and polar angle of Eq. (1) to the raw $I(\mathbf{k})$ intensities of (a). (c) The normalized $\chi(\mathbf{k})$ data set, as determined by the removal of the experimentally derived $I_0(\mathbf{k})$ of (b).

background must be deduced somehow from experimental $I(\mathbf{k})$ intensities, and we do it here by fitting a low-order polynomial in wave vector k and polar angle θ to the full $I(\mathbf{k})$ data set:

$$I_0(\mathbf{k}) = a_{00} + \sum_{m=1}^{3} \sum_{n=1}^{3} a_{mn} k^m \cos[(2n-1)\theta]. \qquad (1)$$

Here, the coefficients a_{mn} are determined by a least-squares fit to $I(\mathbf{k})$. This is qualitatively similar to some prior normalization schemes that subtract $I_0(\mathbf{k})$ as the low-frequency Fourier components of raw $I(\mathbf{k})$ data sets.[9(c),15(a),15(d),23] But this three-dimensional determination of $I_0(\mathbf{k})$ is distinctly different from previous methods for determining $I_0(\mathbf{k})$ in which simple linear, low-order polynomial, or spline fits were separately made for each set of different wave vectors along a given direction: $I_{\hat{k}}(\mathbf{k})$ [Refs. 9(a), 9(c), and 9(d)] or each set of different directions at a given wave vector: $I_k(\hat{\mathbf{k}})$ [Refs. 9(b) and 9(e)]. Such separate normalizations within each scanned-energy or scanned-angle set of data points in $I(\mathbf{k})$ arose from the historical development of photoelectron holography, in which data tended to be collected with **k**-space resolution that was either fine-in-direction/coarse-in-wave vector or coarse-in-direction/fine-in-wave vector.[24] There has, in fact, been a recent proposal to consider these **k**-space sampling choices as distinct holographic atomic structure probes,[9(e)] but these choices simply represent extremes of a continuous range of **k**-space sampling, of which the optimal choice has been shown to be in the intermediate range of roughly equally resolved direction and wave-vector data steps.[20,24] Thus, this distinction[9(e)] seems artificial, and not consistent with the optimal use of the holographic methodology. As a consequence, the normalization of $I(\mathbf{k})$ intensities should ideally be made via the determination of a general $I_0(\mathbf{k})$ background that depends on wave vector and direction [such as that in Eq. (1)], rather than determined separately for each wave vector or direction in the $I(\mathbf{k})$ data set.

Figures 2(b) and 3(b) show the surface and bulk $I_0(\mathbf{k})$ functions as determined by applying the wave vector and polar angle fit of Eq. (1) to the raw surface and bulk photoelectron diffraction $I(\mathbf{k})$ data sets of Figs. 2(a) and 3(a), respectively. Figures 2(c) and 3(c) then show the $\chi(\mathbf{k})$ functions obtained from the raw $I(\mathbf{k})$ intensities of Figs. 2(a) and 3(a), using the wave vector and angle fit $I_0(\mathbf{k})$ of Figs. 2(b) and 3(b). These data points were then remapped onto a grid of $\delta k = 0.1\,\text{Å}^{-1}$ and $(\delta\theta, \delta\phi) = (5°, 5°)$ over the ranges $k = 3.85-7.45\,\text{Å}^{-1}$ ($E = 56-211\,\text{eV}$) and $40° \leq \theta \leq 90°$, for a final total of 6697 unique intensities in the symmetry-reduced 1/4 of the solid angle above the sample. These $\chi(\mathbf{k})$ data steps, while coarser than the data steps of the raw $I(\mathbf{k})$ data sets, are still fine enough to ensure images free of coarse-sampling aliases and aberrations to within ≈6 Å from the emitting sites.[24]

A choice of $(m,n) \leq (3,3)$ for the coefficients used to fit $I_0(\mathbf{k})$ was found to be sufficient to subtract out any detrimental artifacts at the origin, with higher-order (m,n) coefficients for $I_0(\mathbf{k})$ not significantly improving the fidelity of the atomic images in the reconstruction volume of interest. Although some polar-angle dependent structure is noticeable in the surface $I_0(\mathbf{k})$ background of Fig. 2(b), in particular a peak along the normal and a ring at smaller angles, these

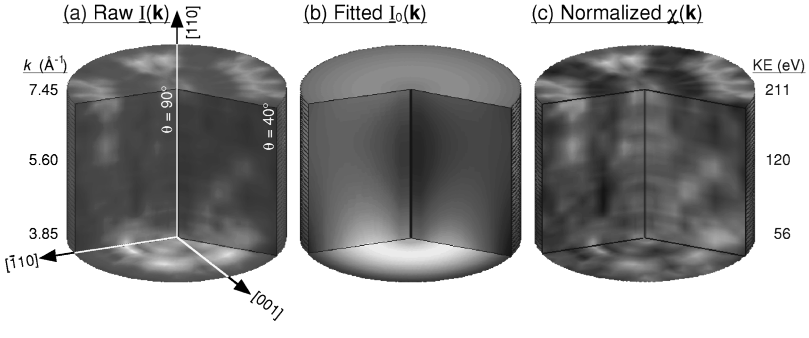

FIG. 3. As Fig. 2, but for bulk W $4f_{7/2}$ emission.

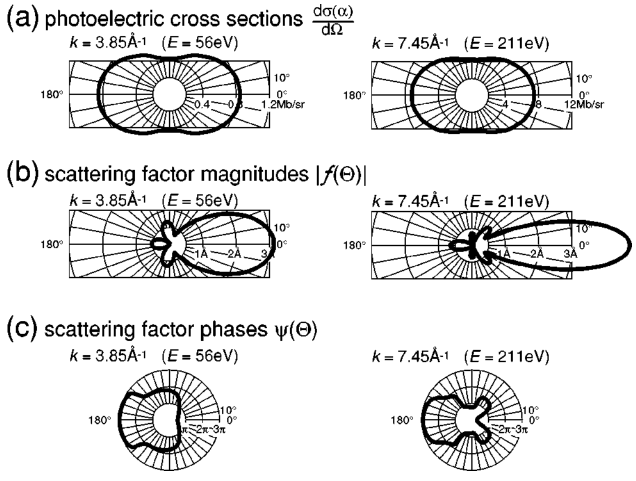

FIG. 4. The angular dependence of important theoretical quantities, as evaluated at the two extreme internal wave vectors (kinetic energies) of the experimental data set: $k_{\text{min}}=3.85\,\text{Å}^{-1}$ ($E=56\,\text{eV}$) and $k_{\text{max}}=7.45\,\text{Å}^{-1}$ ($E=211\,\text{eV}$). (a) The W $4f$ differential photoelectric cross section $d\sigma/d\Omega$, as a function of emission angle with respect to the radiation polarization direction. (b) The W scattering factor magnitude $[|f(\Theta_{\mathbf{r}}^{\mathbf{k}}|]$, as a function of the photoelectron scattering angle $\Theta_{\mathbf{r}}^{\mathbf{k}}$. Here, $\Theta_{\mathbf{r}}^{\mathbf{k}}=0°$ is the forward-scattering direction, and $\Theta_{\mathbf{r}}^{\mathbf{k}}=180°$ is the backscattering direction. (c) The scattering phase shift $\psi(\Theta_r^k)$, again as a function of scattering angle.

features do not transform so as to correspond to any sort of atomic image. (From an experimental point of view, such features can result from purely instrumental effects associated with nonperfect alignment of the focused light beam and the electron spectrometer acceptance on the sample surface.) This was verified by applying the reconstruction algorithm of method A to the $I_0(\mathbf{k})$ data set of Fig. 2(b), which is found to result merely in the expected spurious image intensity at the origin, which is then removed from the final images with the subtraction of $I_0(\mathbf{k})$. Of course, if the sum in Eq. (1) were taken to sufficiently high order, true holographic structure would begin to be removed in subtracting $I_0(\mathbf{k})$, but we are well short of this point in all of our analyses.

III. GENERATION OF THEORETICAL DIFFRACTION PATTERNS

For comparison with experiment, single-scattering and multiple-scattering theoretical models were used to calculate surface and bulk emission $I(\mathbf{k})$'s from W(110) clusters. The Rehr-Albers separable Green's function approach was used to describe the scattering.[26] This was first implemented in photoelectron diffraction calculations by Kaduwela, Friedman, and Fadley,[27] and a faster algorithm employing it has recently been developed by Chen, Wu, and Shirley,[28(a)] and further expanded more recently.[28(b)] The calculations reported here made use of this newer and faster program. The radial matrix elements and phase shifts necessary for describing the primary excitation, as well as the scattering phase shifts, were calculated using the program. Figure 4 shows several of the key physical ingredients of such theoretical calculations, as evaluated at the two extreme energies studied here of $k_{\text{min}}=3.85\,\text{Å}^{-1}$ ($E=56\,\text{eV}$) and $k_{\text{max}}=7.45\,\text{Å}^{-1}$ ($E=211\,\text{eV}$): (a) the W $4f$ differential photoelectric cross sections $d\sigma/d\Omega$, and W-atom scattering factor (b) magnitudes $|f(\Theta_r^k)|$ and (c) phases $\psi(\Theta_r^k)$. As a first point, the differential cross section is reasonably isotropic over this energy range, suggesting that photoelectron *source-wave* anisotropies should not affect holographic images too seriously. However, a correct allowance for such source-wave effects would also deal with the amplitudes and phases of the *d* and *g* final-state channels involved,[29] leading to potentially more complex effects on holographic images that we will not consider here. As far as *scattered-wave* effects are concerned, it is clear that both the W scattering factor magnitudes and phases of Figs. 4(b) and 4(c) are strongly anisotropic compared to the more ideal scattering nature of x rays,[19,22] and that these anisotropies could adversely affect the resulting reconstructed atomic images, introducing aberrations and position shifts.[16–18] We will consider correcting for such scattered wave effects below.

The clusters used for simulating surface and bulk emission considered here consisted of 72 and 64 atoms, respectively, and were chosen in order to include all events down to a 2% cutoff of all multiple-scattered wave-front contributions to the detected intensity in the far field.[25] Debye-Waller effects based on correlated vibrations and corresponding to a sample temperature of 300 K were included, as were inelastic attenuation effects, with the inelastic attenuation lengths calculated using the method developed by Tanuma, Powell, and Penn,[30] and ranging from 1.71 Å at $k_{\text{min}}=3.85\,\text{Å}^{-1}$ to 4.42 Å at $k_{\text{max}}=7.45\,\text{Å}^{-1}$. The detector full angle of acceptance was taken to be 3°, and the geometry between the incident radiation polarization, sample, and detector was identical to the experimental setup of Fig. 1(a). These theoretical photoemission intensities were then also normalized using the wave vector and direction normalization scheme of Eq. (1).

IV. DETERMINATION OF ATOMIC IMAGES FROM EXPERIMENTAL AND THEORETICAL $\chi(\mathbf{k})$ DATA SETS

Once the normalized holographic $\chi(\mathbf{k})$ intensities have been obtained from either experiment or theory, atomic images $U(\mathbf{r}')$ can then be reconstructed via several methods that we now review. The simplest of these is denoted here as method A:[3]

$$U_A(\mathbf{r}')\equiv\int\int\int_K d\mathbf{k}\,e^{-i(\mathbf{k}\cdot\mathbf{r}'-kr')}\chi(\mathbf{k}), \tag{2}$$

and it is a deconvolution transform with a path-length-difference kernel $e^{i(\mathbf{k}\cdot\mathbf{r}'-kr')}$, with K representing the appropriate limits on emission angle and wave-vector magnitude. This kernel assumes an outgoing source wave of *s* character, weak *s*-wave electron-atom scattering, and a negligible, or at least small, scattering phase shift, and can be thought of as an ''optical'' limit. In this limit, this transform should reconstruct the atomic scattering field at relative positions $\mathbf{r}'$ surrounding the emitter.[3,22] An additional important property of this method is that, in being a transform over a volume in $\mathbf{k}$ space (i.e., over both direction and wave vector), it suppresses both twin-image and multiple-scattering effects, as first pointed out by Barton and co-workers[3(a),3(b)] and subse-

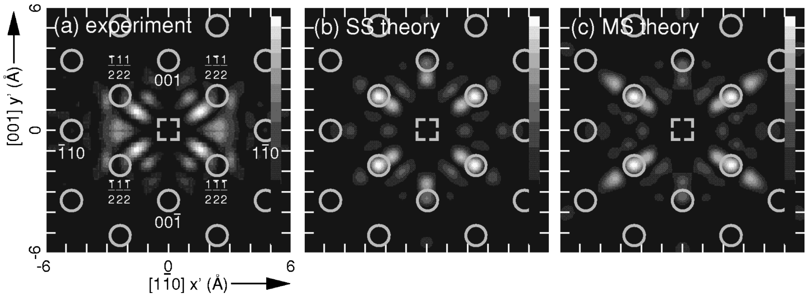

FIG. 5. W(110) atomic images obtained from experimental and theoretical W $4f$ surface-emission $\chi(\mathbf{k})$ data sets, in the horizontal (110) plane, via method A. The surface emitter site at the origin is indicated by dashed squares, and the known positions of the scatterers are indicated by circles. The nearest and next-nearest scattering positions have been labeled in panel (a). Axes are marked off in 1-Å units. Image intensities for $z \leqslant -3.5$ Å have been rescaled, with the scale factors indicated on the figures. (a) Image reconstructed from the experimental $\chi(\mathbf{k})$ data set of Fig. 2(c). (b) Image reconstructed from a theoretical single-scattering $\chi(\mathbf{k})$ data set. (c) Image reconstructed from a theoretical multiple-scattering $\chi(\mathbf{k})$ data set.

quently by Tong *et al.*[3(c)] However, due to the nonideal nature of electron emission and scattering, atomic images obtained via method A have still been found to suffer from aberrations, artifacts, and position shifts.[16–18] Nonetheless, such images can be of good enough quality to allow an initial and useful determination of atomic structure.[9–13]

Figures 5 and 6 show the reconstructed images in the horizontal (110) and vertical $(\overline{1}1\overline{2})$ planes, respectively, obtained from applying method A [Eq. (2)] to (a) the experimental surface emission $\chi(\mathbf{k})$ of Fig. 2(c); (b) a theoretical single-scattering surface emission $\chi(\mathbf{k})$; and (c) a theoretical multiple-scattering surface emission $\chi(\mathbf{k})$. The $(\overline{1}1\overline{2})$ plane was chosen to pass through the nearest-neighbor atoms to a given emitter that lie in the horizontal (110) surface plane, as these would presumably also be the strongest atoms in the holographic images. The emitter position is indicated by a dashed square, and the ideal positions of the neighboring atoms are indicated by circles. The expected atomic image resolution for this wave vector and angular range of $\chi(\mathbf{k})$ in the horizontal $[\overline{1}11]$ direction is given by $\delta x \approx \pi/\Delta k_x \equiv \pi/[2k_{\max}\sin(\theta_{\max}-\theta_{\min})] \approx 0.3$ Å, and in the vertical [110] direction is given by $\delta z \approx \pi/\Delta k_z \equiv \pi/[k_{\max}-k_{\min}\cos(\theta_{\max}-\theta_{\min})] \approx 0.6$ Å,[23] and these numbers are comparable to the actual atomic image dimensions in Figs. 5 and 6. As noted above, Eq. (2) makes no special effort to suppress aberrations due to the nonoptical nature of the electron-scattering process. In all of the images in Fig. 6, the backscattering atom along $\overline{1}\overline{1}0$ and the $\frac{1}{2}\overline{\frac{1}{2}}\overline{\frac{1}{2}}$ and $\overline{\frac{1}{2}}\overline{\frac{1}{2}}\frac{1}{2}$ side scattering atoms are reasonably well resolved, with experiment and the more accurate multiple-scattering theory showing the sharpest features for the backscattering atoms, and agreeing very well with one another. In the experimental image of Figs. 5(a) and 6(a), the $\frac{1}{2}\overline{\frac{1}{2}}\overline{\frac{1}{2}}$ and $\overline{\frac{1}{2}}\overline{\frac{1}{2}}\frac{1}{2}$ atoms are shifted in toward the emitter (by ≈0.7 Å), and downward from the $z=0$ Å surface (by ≈0.2 Å); this is perhaps due to the strong anisotropies of the atomic-scattering factor and its phase shift for such side-scattering directions [cf. Figs. 4(b) and 4(c)]. As expected, the backscattering $\overline{1}\overline{1}0$ atom is better resolved due to the more ideal nature of electron backscattering [approximately constant amplitude and phase shift, as shown also in Figs. 6(b) and 6(c)], with no significant position shift.[6(a),6(b)] The experimental backscattering image is also less intense (≈50%) than the side-scattering atomic images; and image intensities above and below $z=-3.5$ Å have been scaled accordingly (with scale factors indicated directly on each panel). This difference in relative image intensity is qualitatively expected due to both the angular dependence in the scattering factor amplitude for lower energies [cf. Fig. 4(b)] and the longer inelastic attenuation path of the wave front that illuminates, and is subsequently scattered by, the backscattering atom, as compared to the wave-front paths that involve the side-scattering atoms. Despite these position shifts and aberrations, this experimental atomic image overall gives excellent *ab initio* estimates of the positions of the backscattering atoms surrounding the surface W(110) emitter and good estimates of the positions of the side-scattering atoms, which could, in principle, then be refined e.g. using *R*-factor comparisons of experiment with model diffraction calculations for various structures.[9(c),21,31]

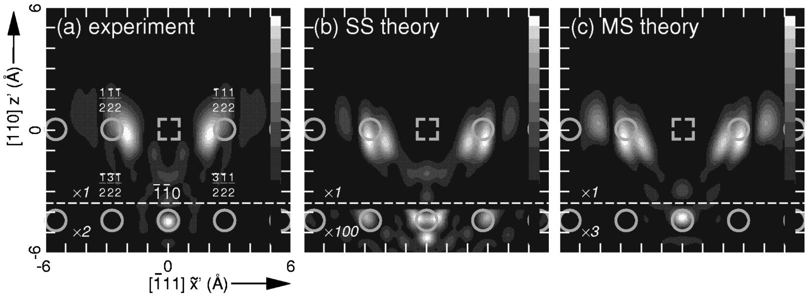

FIG. 6. As Fig. 5, but for the vertical $(\overline{1}1\overline{2})$ plane. The positions of the scatterers (assuming no surface relaxation) are indicated by circles.

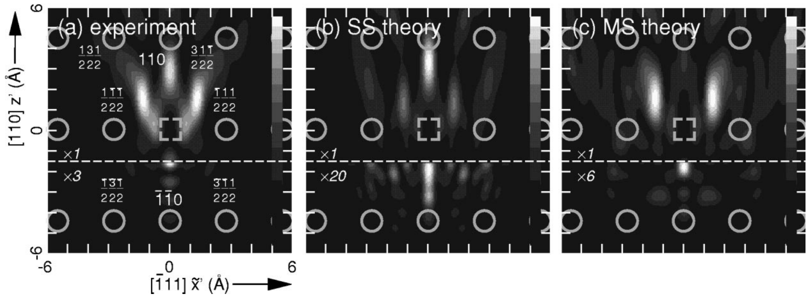

FIG. 7. W(110) atomic images obtained from experimental and theoretical W $4f$ bulk emission $\chi(\mathbf{k})$ data sets, in the vertical $(\bar{1}1\bar{2})$ plane, via method A. The bulk emitter site at the origin is indicated by dashed squares, and the positions of the scatterers are indicated by circles. The nearest and next-nearest scattering positions have been labeled in panel (a). Axes are marked off in 1-Å units. Image intensities for $z \leqslant -1.5$ Å have been rescaled, with the scale factors indicated on the figures. (a) Image reconstructed from the experimental $\chi(\mathbf{k})$ data set of Fig. 3(c). (b) Image reconstructed from a theoretical single-scattering $\chi(\mathbf{k})$ data set. (c) Image reconstructed from a theoretical multiple-scattering $\chi(\mathbf{k})$ data set.

The single- and multiple-scattering images of Figs. 6(b) and 6(c) are similar to experiment in that the $\frac{1}{2}\overline{\frac{1}{2}}\overline{\frac{1}{2}}$ and $\overline{\frac{1}{2}}\frac{1}{2}\frac{1}{2}$ side scatterers exhibit side lobes that are shifted in towards the emitter, and downward from the surface. However, the theoretical side-scattering atomic images of Figs. 6(b) and 6(c) differ from those of Fig. 6(a) in that the theoretical image peaks are split. This splitting may be due to a number of reasons, among them the differences between the theoretical and actual photoemitted source-wave angular distributions and atomic-scattering factors. Yet, these single- and multiple-scattering models produce other image features that rather closely match the experimental image of Fig. 6(a) in the side-scattering region, even including the faint aberrations seen at $(x,z) \approx (\pm 4\,\text{Å}, 0\,\text{Å})$. The most marked difference between the experimental image of Fig. 6(a) and the single-scattering image of Fig. 6(b) is the triply split backscattering $\overline{1}\overline{1}0$ atom in the latter, which is also very much weaker in intensity (≈1%) relative to the side scattering $\frac{1}{2}\overline{\frac{1}{2}}\overline{\frac{1}{2}}$ and $\overline{\frac{1}{2}}\frac{1}{2}\frac{1}{2}$ peaks. This difference must be primarily due to the oversimplification of the single-scattering model, as seen by comparing Figs. 6(b) and 6(c), for which the agreement is excellent. For example, in the multiple-scattering image of Fig. 6(c), the backscattering $\overline{1}\overline{1}0$ peak intensity relative to the side scattering $\frac{1}{2}\overline{\frac{1}{2}}\overline{\frac{1}{2}}$ and $\overline{\frac{1}{2}}\frac{1}{2}\frac{1}{2}$ peaks (≈33%) is very close to that of Fig. 6(a) (≈50%). This dramatic difference between single and multiple scattering can arise because each of the atoms in the multiple-scattering model becomes an emitter, which can then illuminate the atoms surrounding it, especially the atom located at the $\overline{1}\overline{1}0$ relative position. In this way more scattering events contribute to the backscattering signal in the resulting holographic $\chi(\mathbf{k})$ intensities, and as such the reconstructed $\overline{1}\overline{1}0$ atomic intensity can be much stronger for the image reconstructed from the multiple-scattering model than that from the single-scattering model. Thus, the closer match between Fig. 6(c) and the experimental image of Fig. 6(a) graphically illustrates that multiple-scattering more accurately describes the nature of the creation of the experimental holographic photoelectron intensities $I(\mathbf{k})$. This is all the more noteworthy in view of the fact that such a multiple wave-vector volume transform is known to suppress multiple-scattering effects,[3(b)] obviously there is not a complete suppression, even with this large data set.

Atomic images were also reconstructed from the experimental bulk emission $\chi(\mathbf{k})$ of Fig. 3(c), as well as from theoretical single- and multiple-scattering bulk emission $\chi(\mathbf{k})$'s. Figures 7–9 show these experimental and theoretical images reconstructed via method A [Eq. (2)] in the vertical $(\bar{1}1\bar{2})$, $(\bar{1}10)$, and (001) planes, respectively. Immediately apparent in all of the experimental and theoretical images of Figs. 7–9(a) is the lack of a clear backscattering $\overline{1}\overline{1}0$ atomic image. The faint features spaced at ≈0.9 Å intervals along the $[\overline{1}\overline{1}0]$ direction are, in fact, alias peaks that arise from the Fourier transformlike properties of Eq. (2).[24] Because of the finite amount of volume enclosed by the $\chi(\mathbf{k})$ data set in $\mathbf{k}$ space, these spurious peaks are expected at $\pi/(k_{\max}-k_{\min}) = \pi/(7.45-3.85\,\text{Å}^{-1}) = 0.871\,\text{Å}$ intervals along low-index backscattering directions (i.e., $[\overline{1}\overline{1}0]$). These alias peaks are

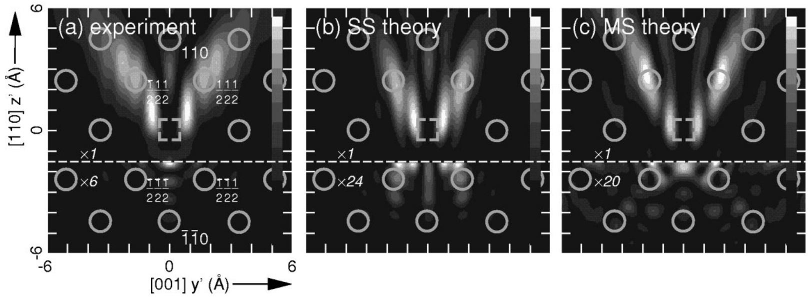

FIG. 8. As Fig. 7, but for the vertical $(\bar{1}10)$ plane.

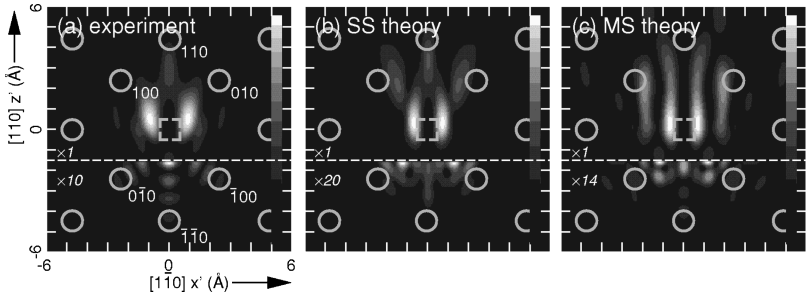

FIG. 9. As Fig. 7, but for the vertical (001) plane.

also faintly evident along the $[0\bar{1}0]$ and $[\bar{1}00]$ directions in the experimental (001) plane image of Fig. 9(a). Aside from these alias backscattering peaks, no appreciable backscattering or side-scattering atomic images are seen in the experimental images of Figs. 7–9(a), as well as the theoretical images of Figs. 7–9(b) and 9(c). This is simply due to the much stronger forward-scattering amplitudes, which causes the contribution of the forward-scattering atoms to dominate the $\chi(\mathbf{k})$ intensities, thus leading them to be preferentially imaged, as seen in previous studies of bulk Cu(001).[32] The form of the scattering-factor amplitudes in Fig. 4(b) makes it clear why this is true as well: forward scattering is ~6–8 times stronger than back scattering over the energy interval involved here. As expected from the comparison of the experimental and theoretical surface-emission images above, the relative intensities of the experimental backscattering images for the bulk emission case (even though for the most part merely artifactual) are better reproduced in the multiple-scattering model images of Figs. 7(c)–9(c), as the relative backscattering intensities in the single-scattering images of Figs. 7(b)–9(b) are much weaker.

Considering now the image features in the forward-scattering directions, we note that, for the $(\bar{1}1\bar{2})$ plane images of Fig. 7, there are three forward-scattering artifacts in the experimental image of Fig. 7(a), approximately 3 Å from the emitter and along the [131], [110], and $[31\bar{1}]$ directions, which do not correspond to actual atomic locations. These artifacts are weak compared to the features seen in the other $(\bar{1}10)$ and (001) plane images of Figs. 8 and 9. That is, these artifacts in the $(\bar{1}1\bar{2})$ plane are only ≈3 times more intense than the backscattering alias peaks discussed above, compared to the forward-scattering features in the $(\bar{1}10)$ and (001) planes, which are, respectively, ≈6 and ≈10 times more intense than the backscattering alias peaks. The artifact along the [110] direction can be seen in the single-scattering image of Fig. 7(b), and faint indications of the [131] and $[31\bar{1}]$ artifacts can also be found. The artifacts along the [131] and $[31\bar{1}]$ directions dominate the multiple-scattering image of Fig. 7(c), but the artifact along the [110] direction is now only faintly discernible. Thus, the single- and multiple-scattering images are in reasonably good agreement with the experimental image of Fig. 7(a), differing only in the relative intensities of the artifacts along the [110], [131], and $[31\bar{1}]$ directions.

The differences between the experimental, single- and multiple- and forward-scattering atomic images in the $(\bar{1}10)$ and (001) planes (Figs. 8 and 9) are less apparent than for the case of the $(\bar{1}1\bar{2})$ plane images of Fig. 7. Note here that the $(\bar{1}10)$ plane is special for a bulk emitter in that it contains the nearest-neighbor forward-scattering atoms that are expected to be the strongest features in the holographic images. Previous studies have demonstrated that single-scattering models can adequately reproduce the features seen in forward-scattering atomic images reconstructed from bulk systems, even though they often exhibit elongation roughly parallel to the scattering direction,[9(a)] but we see here that the bulk atomic images reconstructed from multiple-scattering models do not differ greatly from images obtained from experiment and single-scattering models. This could be due to both inelastic attenuation and elastic scattering of the photoelectron wave fronts, such that higher-order multiple-

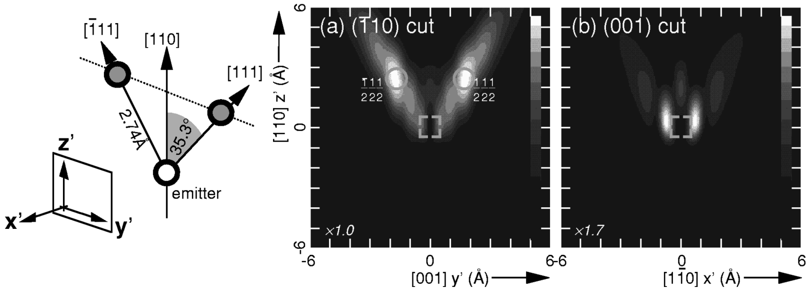

FIG. 10. Simple $\frac{\bar{1}}{2}\frac{\bar{1}}{2}\frac{1}{2}$ and $\frac{1}{2}\frac{1}{2}\frac{1}{2}$ forward-scattering W cluster, for which images have been derived as: (a) Atomic image obtained from a theoretical single-scattering W $4f\chi(\mathbf{k})$ data set calculated for this cluster, in the vertical $(\bar{1}10)$ plane, via method A. The emitter site at the origin is indicated by dashed squares, and the positions of the scatterers are indicated by circles. Axes are marked off in 1-Å units. Image intensities have been rescaled relative to the same standard maximum in this panel (=1.0) for both Figs. 10 and 11, with the scale factors indicated. (b) As (a), but in the (001) plane and with a scale factor of 1.7.

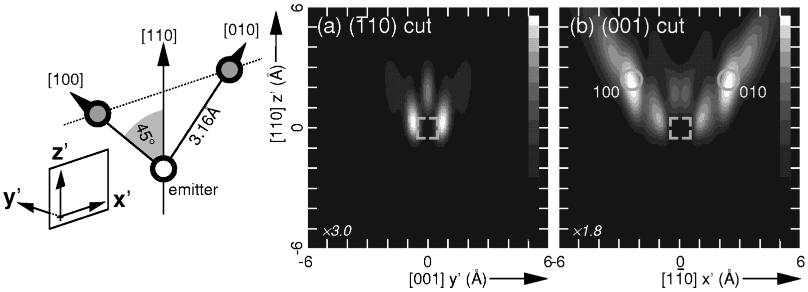

FIG. 11. As Fig. 10, but for a 100 and 010 forward-scattering W cluster. (a) Image in the vertical ($\bar{1}$10) plane, with a scale factor of 3.0. (b) Image in the vertical (001) plane, with a scale factor of 1.8.

scattering events deep in the bulk do not contribute much to the $I(\mathbf{k})$ intensities measured above the sample; instead, the majority of the $I(\mathbf{k})$ signal that originates from deeply buried emitters comes from lower-order multiple-scattering events.[33]

Note also that the only nearest-neighboring forward-scattering atoms imaged in *any* of these experimental or theoretical bulk-emission images are the $\overline{\tfrac{1}{2}}\tfrac{1}{2}\tfrac{1}{2}$ and $\tfrac{1}{2}\tfrac{1}{2}\tfrac{1}{2}$ atoms, as seen in the ($\bar{1}$10) plane images of Fig. 8. Neither the 100 or the symmetry-equivalent 010 forward-scattering atoms are visible in the experimental or theoretical (001) plane images of Fig. 9. The cause of this preferential imaging of the ($\bar{1}$10) plane atoms, as well as the strong double-peak artifacts near the origin in the ($\bar{1}$10) and (001) planes, located in the horizontal (110) plane of the emitter and approximately 0.7 Å away from the emitter, is discussed below.

As noted before, Fig. 4(b) shows the W scattering-factor magnitudes for $k_{\text{min}}=3.85\,\text{Å}^{-1}$ and $k_{\text{max}}=7.45\,\text{Å}^{-1}$ photoelectrons. Note that the forward-scattering peak is quite narrow, having a half angle at half-maximum amplitude of approximately 30° for $k_{\text{min}}=3.85\,\text{Å}^{-1}$ photoelectrons, and approximately 15° for $k_{\text{max}}=7.45\,\text{Å}^{-1}$ photoelectrons. While it is the presence of these forward-scattering peaks that causes the preferential scattering from, and subsequent imaging of, forward-scattering atoms, we demonstrate more quantitatively in Figs. 10 and 11 how this narrow angular width of the forward-scattering peak also causes the preferential imaging of forward-scattering atoms nearest to the azimuthal axis (i.e., the surface normal) of the $\chi(\mathbf{k})$ data set.

The panels to the left of Figs. 10(a) and 11(a) show the geometry of two small W clusters. The geometry for Fig. 10 is a single W photoemitter, with only $\overline{\tfrac{1}{2}}\tfrac{1}{2}\tfrac{1}{2}$ and $\tfrac{1}{2}\tfrac{1}{2}\tfrac{1}{2}$ W scatterers in the ($\bar{1}$10) plane. The geometry for Fig. 11 is a single W photoemitter, with only 100 and 010 forward-scattering atoms in the (001) plane. Single-scattering $\chi(\mathbf{k})$ intensities were calculated for both of these simple W clusters, and images reconstructed from these theoretical $\chi(\mathbf{k})$ data sets using method A in the ($\bar{1}$10) and (001) planes are shown in Figs. 10(a) and 10(b) and 11(a) and 11(b), respectively. The intensities of all the images of Figs. 10(a) and 10(b) and 11(a) and 11(b) have been rescaled relative to each other to yield the same maximum-to-minimum gray scale; these relative scale factors are indicated on each image, with that in the most intense image of Fig. 10(a) being arbitrarily set to 1.0.

Figures 10(a) and 10(b) show the ($\bar{1}$10) and (001) plane image reconstructions of the cluster with only $\overline{\tfrac{1}{2}}\tfrac{1}{2}\tfrac{1}{2}$ and $\tfrac{1}{2}\tfrac{1}{2}\tfrac{1}{2}$ scatterers. Note that while the $\overline{\tfrac{1}{2}}\tfrac{1}{2}\tfrac{1}{2}$ and $\tfrac{1}{2}\tfrac{1}{2}\tfrac{1}{2}$ atomic images are clearly and strongly visible in the ($\bar{1}$10) plane containing these atoms, these atoms produce spurious images in the (001) plane, notably the strong features located approximately 0.7 Å to either side of the emitter along the horizontal (110) plane. Figures 11(a) and 11(b) show the ($\bar{1}$10) and (001) plane image reconstructions of the cluster with only 100 and 010 scatterers. The 100 and 010 atomic images are again clearly visible in the (100) plane containing these atoms, and these atoms also produce similar near-emitter artifacts in the ($\bar{1}$10) plane. These near-emitter artifacts are also similar to those that appear in the experimental and theoretical bulk-emitter images of Figs. 7–9. These near-emitter artifacts are thus not caused by incomplete $I(\mathbf{k})$ background subtraction, but are simply extraneous reconstructed features of the forward-scattering $\overline{\tfrac{1}{2}}\tfrac{1}{2}\tfrac{1}{2}$, $\tfrac{1}{2}\tfrac{1}{2}\tfrac{1}{2}$, 100, and 010 atoms.

Note also that the 100 and 010 atomic images in the (001) plane [Fig. 11(b)], are ~1.8 times less intense than those of the $\overline{\tfrac{1}{2}}\tfrac{1}{2}\tfrac{1}{2}$ and $\tfrac{1}{2}\tfrac{1}{2}\tfrac{1}{2}$ atomic images in the ($\bar{1}$10) plane [Fig. 10(a)]. This can be understood from the narrowness of the forward-scattering maxima of the W scattering factor, as shown in Fig. 4(b). Since the $\chi(\mathbf{k})$ data set spans a polar-angle range of $40° \leqslant \theta \leqslant 90°$ as measured within the surface, this means that the strong forward-scattering diffraction features of the $\overline{\tfrac{1}{2}}\tfrac{1}{2}\tfrac{1}{2}$ and $\tfrac{1}{2}\tfrac{1}{2}\tfrac{1}{2}$ atoms (which lie along the [$\bar{1}$11] and [111] directions) will be well within this polar-angle range, as the angle between [$\bar{1}$11] (or [111]) and the normal [110] direction is $\theta^{[110]}_{[111]} \approx 35.3°$. In contrast, nearly half of the forward-scattering diffraction features of the 100 and 010 atoms (which lie along the [100] and [010] directions) will be outside of this polar-angle range, as the angle between [100] (or [010]) and the normal [110] direction is $\theta^{[110]}_{[100]} = 45°$.

Thus, the preferential imaging of the nearest-neighbor $\overline{\tfrac{1}{2}}\tfrac{1}{2}\tfrac{1}{2}$ and $\tfrac{1}{2}\tfrac{1}{2}\tfrac{1}{2}$ forward scatterers can be understood by the localization of their strongest forward-scattering diffraction features within the polar-angle range of this $\chi(\mathbf{k})$ data set.[16,17] The absence of the atomic images of the 100 and 010 forward-scattering atoms in Fig. 9 is merely due to a portion of their forward-scattering diffraction features lying outside the polar-angle range of this $\chi(\mathbf{k})$ data set. This also explains the total absence of any side-scattering atomic-image features, as their forward-scattering diffraction features lie well outside of the polar-angle range of the $\chi(\mathbf{k})$ data set. Any low-energy photoelectron diffraction data set is thus expected to exhibit qualitatively similar effects due to electron refraction at the innerpotential surface barrier, even if the experimental data is initially taken down to very low takeoff angles with respect to the surface.

Thus, imaging forward-scattering atoms are dependent on whether their strong forward-scattering diffraction features lie within the $\chi(\mathbf{k})$ data-set polar-angle range. In addition, due to the strong, nonoptical nature of forward scattering [nonconstant amplitude and phase shift, as shown in Figs. 4(b) and 4(c)], these forward-scattering atomic images are expected to be less ideal than those of backscattering atoms. For imaging backscattering atoms from overlayer and surface systems, it has thus been shown to be of benefit to exclude the forward-scattering regions of the surface and near-surface plane atoms, in order to retrieve only the more ideal optical backscattering information of atoms that lie more nearly below emitter sites.[5] More recently, there has also been a proposal to image even forward-scattering atoms by means of their more ideal side-scattering contributions, by experimentally keeping the angle between the incident polarized radiation and the photoelectron detector small, such that the detector is kept near the photoexcitation cross-section node that exists, for example, for emission from *s* subshells, and to a lesser degree for emission from non-*s* subshells.[34] This has the effect of suppressing the strong contribution of forward scattering, and putting more emphasis on the side-scattering contributions from these forward-scattering atoms. However, it is clear that this method would not work for all atoms, levels, and wave vectors, as the photoelectric cross sections for W in Fig. 4(a) are very nearly uniform in amplitude.

V. COMPARISON OF ATOMIC IMAGES OBTAINED FROM DIFFERENT RECONSTRUCTION ALGORITHMS

There have been various modifications to the basic optical-reconstruction algorithm of method A [Eq. (2)], and to the definition of the reconstruction integral itself, in order to account for the nonoptical nature of electron scattering, of which four methods will be discussed here. The first of these, which we will call method $\tilde{\mathrm{A}}$, is a straightforward attempt to remove the effects of the complex electron-scattering factor $f(\Theta^{\mathbf{k}}_{\mathbf{r}'})$ by dividing it out in the transform kernel. This has been termed the scattered-wave included Fourier transform by Tonner *et al.*,[4] and it can be written as

$$U_{\tilde{A}}(\mathbf{r}')\equiv\int\int\int_K d\mathbf{k}\,\frac{e^{-i(\mathbf{k}\cdot\mathbf{r}'-kr')}}{f(\Theta^{\mathbf{k}}_{\mathbf{r}'})}\chi(\mathbf{k}). \tag{3}$$

Carrying out this transform implies knowing the identity of the scatterer to be imaged in each region of space, so that $f(\Theta^{\mathbf{k}}_{\mathbf{r}'})$ can be uniquely defined. For the present case, this is trivial, since all scatterers are W atoms and can be assumed to be identical. [A more refined treatment might consider surface atoms to have a different scattering factor, since they are not uniformly surrounded by neighbors, but this type of correction has not been found to be necessary in the analysis of LEED data over a similar energy range.[21(b)]] We note here also that we have not allowed for any effects due to inelastic attenuation or vibrational (Debye-Waller) effects, although these could, in principle, also be included in a more general type of $f(\Theta^{\mathbf{k}}_{\mathbf{r}'})$. An additional effect that could be included in a more general $f(\Theta^{\mathbf{k}}_{\mathbf{r}'})$ is an anisotropy in the outgoing photoelectron wave (source-wave anisotropy), but the cross sections in Fig. 4(a) do not make this seem like a major correction for the case at hand.

A second method (method B) for improving atomic-image fidelity is to utilize only the **k**-space regions in $\chi(\mathbf{k})$ where the photoemitted source wave is most stationary, and the electron $f(\Theta^{\mathbf{k}}_{\mathbf{r}'})$ is most optical-like for specific atomic positions. This general approach was first used in high-energy photoelectron holography of near-forward scattering atoms by Thevuthasan *et al.*,[5] but it has more recently been applied to low-energy studies of backscattering atoms by Tong *et al.*,[6(a)] and Wu and Lapeyre.[6(b)] Since the electron-scattering factor magnitude and phase are roughly constant for backscattering directions ($\Theta^{\mathbf{k}}_{\mathbf{r}'}\approx180°$),[6,22] $\chi(\mathbf{k})$ regions in a cone of half-angle $\alpha\approx30°$ centered on $\hat{\mathbf{k}}=-\hat{\mathbf{r}}'$ directions are used in reconstructing atoms directly beneath the photoemitter site. For the present case, as illustrated in Figs. 4(b) and 4(c), these simplifying assumptions are at least partly true: the magnitude of f is actually fairly strongly varying in the backscattering direction, but the phase Ψ is quite constant. Thus, this ‘‘small-cone’’ algorithm uses the usual optical reconstruction kernel $e^{i(\mathbf{k}\cdot\mathbf{r}'-kr')}$, but as multiplied by a window function $w(\Theta^{\mathbf{k}}_{-\mathbf{r}'})$, which is equal to unity when $\Theta^{\mathbf{k}}_{-\mathbf{r}'}\leqslant\alpha$, and is zero elsewhere in **k** space:

$$U_B(\mathbf{r}')\equiv\int\int\int_K d\mathbf{k}\,e^{-i(\mathbf{k}\cdot\mathbf{r}'-kr')}w(\Theta^{\mathbf{k}}_{-\mathbf{r}})/\chi(\mathbf{k}). \tag{4}$$

A Hanning window function of the form $w_{\mathrm{Hanning}}(\Theta^{\mathbf{k}}_{-\mathbf{r}'})\equiv\cos^2(\pi\cdot\Theta^{\mathbf{k}}_{-\mathbf{r}'}/\alpha)$ has been used in some implementations of Eq. (4),[6(c),6(d)] but here, as in the first uses of method B,[9(a),9(b)] the step function $w(\Theta^{\mathbf{k}}_{-\mathbf{r}'})$ window function was used.

A third algorithm (method C) due to Rous and Rubin[7] recognizes the quantum-mechanical nature of the electron wave front propagating in the bulk, and describes it in terms of the Lippman-Schwinger equation and the first Born approximation. In the form that can be most directly related to Eq. (2), this quantum mechanically based reconstruction algorithm is given by:

$$U_C(\mathbf{r}')\equiv\frac{d}{dr}\left\{r'\,\mathrm{Re}\left[\int\int\int_K d\mathbf{k}\,e^{-i(\mathbf{k}\cdot\mathbf{r}'-kr')}\chi(\mathbf{k})\right]\right\}. \tag{5}$$

Here, the integral on $K\equiv d\mathbf{k}$ is just $U_A(\mathbf{r}')$, but additional operations are performed on its real part only in arriving at $U_C(\mathbf{r}')$.

The final reconstruction algorithm (method D) considered here is due to Hoffman *et al.*[8(a)] and is not strictly speaking holographic in nature. But it is a so-called ‘‘direct method’’ for analyzing photoelectron diffraction data so as to estimate atomic positions, usually of backscattering atoms under adsorbates.[8(b)] Its form is given by

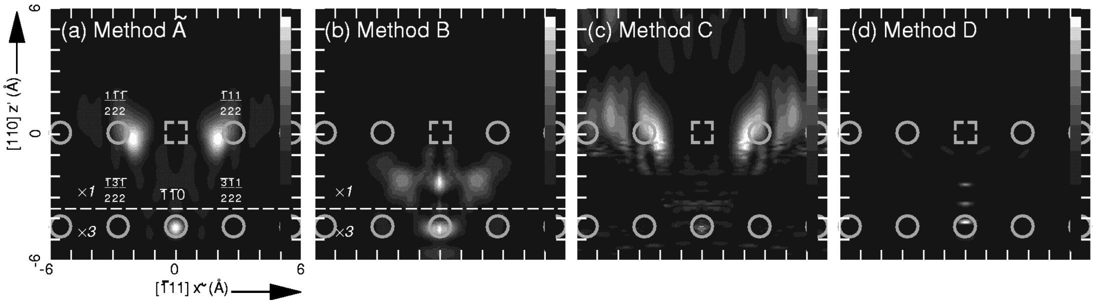

FIG. 12. W(110) atomic images obtained in the vertical $(\overline{1}1\overline{2})$ plane from the experimental W 4f surface emission $\chi(\mathbf{k})$ data set of Fig. 2(c), via methods $\widetilde{A}-$D, as defined in the text. (a) Method $\widetilde{A}$. (b) Method B. (c) Method C. (d) Method D. The surface-emitter site at the origin is indicated by dashed squares, and the positions of the scatterers (assuming no surface relaxation) are indicated by circles. The nearest and next-nearest scattering positions have been labeled in panel (a). Axes are marked off in 1-Å units. Image intensities for $z \leqslant -3.5$ Å have been rescaled [with the exception of (c) and (d)], with the scale factors indicated on the figures.

$$U_D(\mathbf{r}') = \sum_{\hat{\mathbf{k}}} \Delta\sigma_{\hat{\mathbf{k}}} \exp\left[r' \int_k dk\, \chi_{\text{theory}}(\mathbf{k},\mathbf{r}')\chi(\mathbf{k}) \right], \quad (6)$$

where $\Delta\sigma_k$ is a weighting factor for data taken along each direction that is usually treated as a constant, and $\chi_{\text{theory}}(\mathbf{k},\mathbf{r}')$ is calculated via a single-scattering model from

$$\chi_{\text{theory}}(\mathbf{k},\mathbf{r}') = \text{Re}\left[\frac{e^{-i(\mathbf{k}\cdot\mathbf{r}'-kr')}}{kr'} f(\Theta^{\mathbf{k}}_{\mathbf{r}'}) \right]. \quad (7)$$

Calculating $\chi_{\text{theory}}(\mathbf{k},\mathbf{r}')$ thus again requires a knowledge of the atomic identity of each scatterer in order for the scattering factor to be uniquely specified. Thus, Eq. (6) is a redefinition of the reconstruction integral of Eq. (2), but it still relies on the orthogonality of a theoretically calculated single-scattering model $\chi_{\text{theory}}(\mathbf{k},\mathbf{r}')$ with the experimental $\chi(\mathbf{k})$, whose exponentiated dot product over $\mathbf{k}$ space as defined above will tend to produce image-intensity peaks at atomic positions. This method inherently assumes individual fine-step scans of intensity with photon energy over the range k of the integral, and then a coarse sum over directions $\hat{\mathbf{k}}$, as weighted ideally by the solid angle $\Delta\sigma_{\hat{\mathbf{k}}}$, which each subtends: that is, this method involves taking data in what can be termed a ''scanned-energy'' mode.

Figures 12(a)–12(d) show the reconstructed atomic images in the vertical $(\overline{1}1\overline{2})$ plane obtained from applying the reconstruction algorithms of Eqs. (3)–(6) (methods Ã–D, respectively) to the experimental *surface* emission $\chi(\mathbf{k})$ of Fig. 2(c), and these can be compared to Fig. 6(a) (method A).

In Fig. 12(a), based upon method Ã [Eq. (3)], the backscattering $\overline{1}\overline{1}0$ image is still less intense than the $\overline{\frac{1}{2}\frac{1}{2}\frac{1}{2}}$ and $\overline{\frac{1}{2}\frac{1}{2}}\frac{1}{2}$ side scatterers, and is surprisingly even more different ($\approx\frac{1}{3}$) compared to the case in Fig. 6(a) ($\approx\frac{1}{2}$) based on method A with no correction for scattering factor. This remaining difference in relative intensity can be explained from the fact that Eq. (3) still does not correct for the difference in the attenuation paths of the wave fronts involving these atomic sites, nor for intensity changes due to vibrational attenuation or multiple scattering, as discussed above. Also, the $\frac{1}{2}\overline{\frac{1}{2}\frac{1}{2}}$ and $\overline{\frac{1}{2}\frac{1}{2}}\frac{1}{2}$ atomic images are still shifted in towards the emitter, and downward, by essentially the same amounts as in the image derived from method A. Thus, the theoretical scattering factor $f(\Theta^{\mathbf{k}}_{\mathbf{r}'})$ may not be sufficiently accurate to describe the actual effective scattering factor for this system (particularly in the side-scattering direction), while other effects involving anisotropies of the source wave, as well as inelastic scattering, vibrational attenuation, and multiple scattering, also may be involved. The potential importance of such additional effects is also illustrated by the fact that the single- and multiple-scattering images of Figs. 6(b) and 6(c), derived from model clusters containing the same theoretical scattering factor used in Eq. (3), do not exactly reproduce the experimental image of Fig. 6(a). However, some weaker image artifacts in the region enclosed by the $\frac{1}{2}\overline{\frac{1}{2}\frac{1}{2}}$, $\overline{\frac{1}{2}\frac{1}{2}}\frac{1}{2}$, and $\overline{1}\overline{1}0$ atoms in Fig. 6(a) have been somewhat suppressed in Fig. 12(a), thus suggesting that the theoretical scattering factor used in Eq. (3) does beneficially account for some of the scattering anisotropy in this system. Further development in the application of method Ã would involve refining the treatment of the theoretical scattering factors (perhaps they are different at the surface, for example), as well as better accounting for the inelastic attenuation of direct and scattered wave fronts (e.g., by using complex phase shifts), explicitly correcting for the wave vector and angular dependence of the photoemitted source wave (including its d and g wave components), and allowing for vibrational effects.

Figure 12(b) shows the reconstructed atomic images obtained via method B [Eq. (4)], where only the holographic surface-atom $\chi(\mathbf{k})$ intensities in a localized angular region of the source wave and images corresponding to more nearly ideal backscattering regions are used in the imaging deconvolution process. Here, the backscattering $\overline{1}\overline{1}0$ image peak does appear to be sharper, but it also has more extended and diffuse wings in this image compared to that of method A in Fig. 6(a). The side scattering $\frac{1}{2}\overline{\frac{1}{2}\frac{1}{2}}$ and $\overline{\frac{1}{2}\frac{1}{2}}\frac{1}{2}$ atomic images in Fig. 12(b) are completely absent, but this is simply due to the fact that the window function $w(\Theta^{\mathbf{k}}_{-\mathbf{r}'})$ with half-angle $\alpha = 30°$ lies outside the angular range of the $\chi(\mathbf{k})$ data set, which spans only $40° \leqslant \theta \leqslant 90°$. Thus, atoms along the side-scattering directions ($\theta = 0°$) simply cannot be imaged from this data set via this method. Nor was this method proposed for imaging side-scattering atoms. The position of the $\overline{1}\overline{1}0$ atom is also essentially unchanged from Fig. 5(a), so there is no apparent advantage in method B for this case as far as

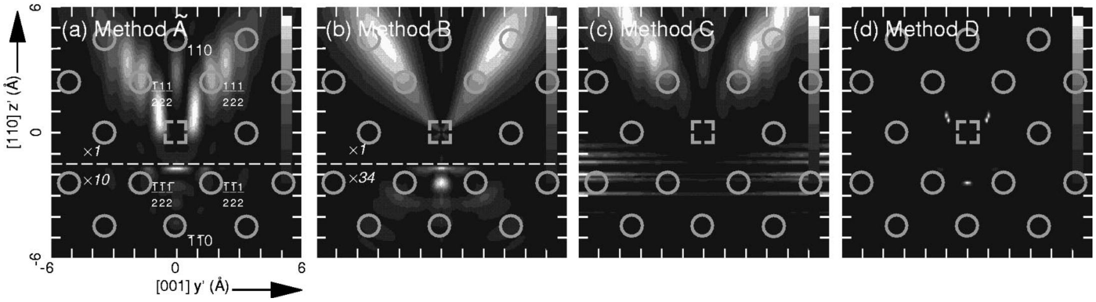

FIG. 13. W(110) atomic images obtained in the vertical $(\overline{1}10)$ plane from the experimental W $4f$ bulk emission $\chi(\mathbf{k})$ data set of Fig. 3(c), via methods $\widetilde{A}-\mathrm{D}$. (a) Method $\widetilde{A}$. (b) Method B. (c) Method C. (d) Method D. The bulk emitter site at the origin is indicated by dashed squares, and the positions of the scatterers are indicated by circles. The nearest and next-nearest scattering positions have been labeled in panel (a). Axes are marked off in 1-Å units. Image intensities for $z \leqslant -1.5$ Å have been rescaled, with the scale factors indicated on the figures [with the exception of (c) and (d)].

locating this atom accurately, even though the method was proposed for more accurately imaging backscattering atoms. The limited size of the window function used in this method also must inherently reduce the resolution of the atomic images, and it is seen to create image aberrations along the low-index directions $[\overline{11}0]$, $[\overline{131}]$, and $[\overline{31}1]$, as seen in a prior analysis of this type of data;[35] these aberrations include an expected broadening of the $\overline{11}0$ atomic image along the $[\overline{1}11]$ direction. However, a positive feature of method B is that it does manage to reconstruct faintly discernible images for the $\overline{\frac{1}{2}\frac{3}{2}\frac{1}{2}}$ and $\overline{\frac{3}{2}\frac{1}{2}\frac{1}{2}}$ backscattering atoms that are barely visible on this gray scale. Thus, method B may be slightly better suited for the refinement of backscattering atomic images, but some loss of image resolution and the appearance of additional artifacts along low-index directions are inherent disadvantages in this approach. It is thus not clear that it has any significant advantage over the straight use of methods A or Ã.

Figure 12(c) shows the reconstructed atomic images obtained via method C [Eq. (5)], where the quantum-mechanical nature of the propagation of electron wave fronts is accounted for in the imaging deconvolution process. The backscattering $\overline{11}0$ atom is a little more sharply defined in this image, but has a position essentially identical to that in Fig. 6(a) as derived using method A. The side scattering $\overline{\frac{1}{2}\frac{1}{2}\frac{1}{2}}$ and $\overline{\frac{1}{2}\frac{1}{2}}\frac{1}{2}$ atomic images are a little less shifted in towards the emitter (by only 0.3 Å), as compared to either Fig. 6(a) or Fig. 12(a). These slight image improvements suggest that not correctly allowing for the propagation of electron wave fronts may account for some of the atomic peak position shifts seen in Figs. 6(a) and 12(a). However, these slight advantages do not compensate the fact that the background level of image artifacts, especially around the forward-scattering atoms, is significantly higher with method C. Thus, although this method certainly deserves further testing with experimental data, it does not appear to have significant advantages over the simple optical transform of method A.

Figure 12(d) shows the reconstructed atomic images obtained via method D [Eq. (6)], which is similar to Eq. (2) in attempting to retrieve the object field $u(\mathbf{r}')$ via an orthogonality relation, but this time between experimental intensities $\chi(\mathbf{k})$ and single-scattering model intensities $\chi_{\mathrm{theory}}(\mathbf{k},\mathbf{r}')$. The backscattering $\overline{11}0$ atom is located fairly well in this image, but it is shifted vertically and does not seem to be as well located as with the other methods discussed previously. The side scattering $\overline{\frac{1}{2}\frac{1}{2}\frac{1}{2}}$ and $\overline{\frac{1}{2}\frac{1}{2}}\frac{1}{2}$ atoms cannot be seen in this image, as the reconstruction algorithm of Eq. (6) best describes the correlation between backscattering $\chi_{\mathrm{theory}}(\mathbf{k},\mathbf{r}')$ and $\chi(\mathbf{k})$ contributions. Because the same atomic electron-scattering factors were used for both methods A and D, the corresponding atomic images of Figs. 12(a) and 12(d) should show corrections for image aberrations and position shifts that are of a comparable degree. It should be noted that method D has been used most successfully in imaging molecular adsorbates on surfaces,[8] where the conditions are probably better described by single-scattering than is the case for the clean W(110) surface considered here. The slight position shift of the $\overline{11}0$ atomic peak can be explained by the W scattering factors used in Eq. (7) and elsewhere in this study [cf. comparable $\overline{11}0$ position shift for the theoretical image in Fig. 6(c)].

Figures 13(a)–13(d) now show the reconstructed atomic images in the same vertical $(\overline{1}10)$ plane obtained from applying the reconstruction algorithms of Eqs. (3)–(6) (methods Ã–D) to the experimental *bulk* emission $\chi(\mathbf{k})$ of Fig. 3(c). These can be compared to Fig. 8(a) (method A). Because methods B and D have been developed specifically to treat backscattering atoms, we do not expect them to perform particularly well for this forward-scattering dominated case, but they are included for completeness and to see whether they are able in any case to resolve something from the backscattering atoms. In Figs. 13(a)–13(d), there are no convincingly strong $\overline{\frac{1}{2}\frac{1}{2}\frac{1}{2}}$ and $\overline{\frac{1}{2}\frac{1}{2}}\frac{1}{2}$ backscattering atomic images visible (except for features that coincide with alias peaks along the $[\overline{11}0]$ direction, as discussed earlier in Figs. 7–9), especially as compared to the stronger forward-scattering image features. Figures 13(c) and 13(d) seem to show no resolvable images for the $\overline{\frac{1}{2}\frac{1}{2}\frac{1}{2}}$ and $\overline{\frac{1}{2}\frac{1}{2}}\frac{1}{2}$ atoms.

Figure 13(a) shows the reconstructed atomic images obtained via method Ã [Eq. (3)]. The forward-scattering features here are not noticeably shifted closer towards their actual locations ($\overline{\frac{1}{2}}\frac{1}{2}\frac{1}{2}$ and $\frac{1}{2}\frac{1}{2}\frac{1}{2}$) as compared to Fig. 8(a) with no scattered-wave correction. This suggests that either the forward-scattering features in this plane are purely artifactual and not associated with an actual atomic image, or that these features are shifted from their actual locations due to additional effects (e.g., source-wave anisotropy, multiple scattering, etc.) that cannot be accounted for by a correction procedure involving single-scattering events.[16,17] A similar closeness in the surface-atom images between methods A and Ã has already been noted in discussing Figs. 6(a) and 12(a), where these additional complicating factors are discussed in more detail. It is also interesting that the lower half of the image with scattered-wave correction is actually weaker ($\cong\frac{1}{10}$) as compared to that with no correction ($\cong\frac{1}{6}$), again qualitatively similar to the surface case. Figure 13(b) shows the reconstructed atomic images obtained via method B [Eq. (4)]. Note that the forward-scattering features are now greatly elongated along the $[\bar{1}11]$ and $[111]$ directions. This is to be expected, as forward-scattering atomic images are much more susceptible than backscattering images to such loss of radial resolution when the solid-angle range of $\chi(\mathbf{k})$ data is limited by the cone defined by $w(\Theta^{\mathbf{k}}_{-\mathbf{r}'})$ (here only 0.27π in width) in reconstructing images using this technique.[3(c),20] This can be contrasted to the larger solid-angle range of the full $\chi(\mathbf{k})$ data set (0.71π) used with methods A, Ã, C, and D. Thus, the radial elongation of the forward-scattering features in Fig. 13(b) suggests that these features are not purely artifactual in origin, but are rather strongly shifted and elongated images of the $\overline{\frac{1}{2}\frac{1}{2}}\frac{1}{2}$ and $\frac{1}{2}\frac{1}{2}\frac{1}{2}$ atoms. One might even propose that they could be useful in locating these atoms in *direction* relative to the emitter, even though they yield no information on *distance* from the emitter. Figure 13(c) shows the reconstructed atomic images obtained via method C [Eq. (5)]. As seen here, method C seems to shift the $\overline{\frac{1}{2}\frac{1}{2}}\frac{1}{2}$ and $\frac{1}{2}\frac{1}{2}\frac{1}{2}$ forward-scattering atomic images away from their actual locations of the atoms, as judged relative to methods A or Ã. These forward-scattering atomic peak-position shifts must arise in some part from inadequately accounting for the quantum-mechanical propagation of electron wave fronts. For example, using the first Born approximation in describing the scattering[7] is quasioptical in its approach.

In contrast to the images obtained from methods Ã–C [Figs. 13(a)–13(c)], the reconstructed atomic image obtained via method D [Fig. 13(d)] shows no forward-scattering features, but instead chiefly manages to retrieve the near-origin artifacts seen in Figs. 8(a) and 13(a). The backscattering image at $z\approx-4.6$ Å is actually related to the alias peak features seen in Figs. 7–9, and Figs. 13(a)–13(b). The lack of forward-scattering atomic images in Fig. 13(d) can be understood by the fact that the integral in Eq. (6) is evaluated over a range of wave vectors, but separately for each different direction. The path-length difference kernel $e^{i(\mathbf{k}\cdot\mathbf{r}'\sim kr')}$ in Eq. (7) can be seen to be identical to unity for forward scatterers (i.e., $\hat{\mathbf{k}}=\hat{\mathbf{r}}'$) along forward-scattering directions, and have less modulations relative to backscatterers for other scattering directions. Thus, the result of Eqs. (6) and (7) is to emphasize backscattering atomic images more so than forward-scattering images. This is what this method was originally formulated to do,[8] and it is evidenced by its success in retrieving the $\overline{11}0$ backscattering atomic peak in Fig. 12(d). This failure of method D to retrieve a backscattering image suggests that the backscattering signal in the bulk emission $\chi(\mathbf{k})$ data set of Fig. 3(c) is far too weak to reconstruct a backscattering atomic image, as compared to the stronger forward-scattering $\chi(\mathbf{k})$ components.

VI. CONCLUDING REMARKS

We have applied five of the currently used direct-imaging algorithms for photoelectron holography to a large high-quality experimental data set from W(110), and to corresponding theoretical simulations of this data set at both the single- and multiple-scattering levels. Separate holograms were measured for both the surface and bulk atoms by making use of the surface core-level shift. The five methods are an ‘‘optical’’ transform over the volume in **k** space spanned by the data (method Ã), the transform of A but with the kernel modified to divide out the electron-atom scattering factor (method A), the so-called ‘‘small-cone’’ transform, which focuses on imaging backscattering atoms (method B), a quantum-mechanically motivated transform (method C), and a nonholographic projection method that also focuses on backscattering atoms (method D). In analyzing the experimental data, we have introduced a general three-dimensional $I_0(\mathbf{k})$ background subtraction scheme in **k** space to better normalize raw $I(\mathbf{k})$ intensities, and compared the three-dimensional atomic images that can be obtained via method A from experiment and theory, and via the five reconstruction algorithms from experiment. The inclusion of multiple scattering in theory is needed with method A to adequately predict the image of the nearest-neighbor backscattering atom.

For a surface-atom emitter, methods A, Ã, and C produce comparable atomic images of backscattering and side-scattering atoms that could then, in principle, be refined for an unknown structure using conventional comparison to theory via *R*-factor refinement. However, method C exhibits considerably more background noise that could hinder image interpretation. In contrast, method B as applied to a surface-atom emitter is somewhat more successful in retrieving backscattering atomic images, but these peaks also suffer from some loss of image resolution, which is inherent for this algorithm, and it is also not possible to image the side-scattering atoms. Thus, it is not clear that method B has a significant advantage in treating this data. Method D produces backscattering images for a surface emitter that are reasonably well defined.

As applied to a bulk emitter for which backscattering, side scattering, and stronger forward scattering can all play a role, all five methods are found to produce poorly resolved forward-scattering images. If peaks are seen at all in this region of image space, they are found to be elongated along the *z* direction and/or the radial direction leading away from the emitter, and to be significantly shifted away from the known atomic positions. Methods A and Ã may have some success with one forward-scattering image (the 110 atom), and method B may be able to determine the *direction* of forward scatterers, but not their distance from the emitter. Method B is able to retrieve faint *backscattering* images from the forward-scattering-dominated bulk emission $\chi(\mathbf{k})$

data set, but it is not clear that these would be sufficiently strong to be useful in an unknown structure.

Overall, we thus find methods A and $\tilde{\mathrm{A}}$ to be the most robust overall for analyzing both surface and bulk $\chi(\mathbf{k})$ data sets from W(110). Imaging backscattering and side-scattering atoms around surface or near-surface emitters is the most promising aspect of photoelectron holography, with the amount of new structural information that can be derived from images of forward-scattering atoms above buried emitters being very limited (at least with the presently available imaging methods). The photoelectron holographic images derived here provide an approximate determination of the structure surrounding the surface-, and to a lesser degree bulk-emission sites of W(110), and suggest the broader applicability of this approach for surface-structure studies. Improving the imaging algorithms to more quantitatively allow for the effects of source-wave anisotropy, inelastic attenuation, and vibrational effects is also desirable and possible. Thus, photoelectron holography holds the promise of providing approximate starting structures to be followed by more conventional structure refinements via multiple-scattering calculations and *R*-factor refinement, with the significant advantage of minimizing search times and avoiding getting trapped in local *R*-factor minima that are not the absolute minima.

ACKNOWLEDGMENTS

We gratefully acknowledge the support of the Office of Naval Research (Contracts Nos. N00014-90-5-1457 and N00014-94-1-0162), the Director, Office of Energy Research, Office of Basic Energy Sciences, Material Sciences Division of the U.S. Department of Energy (Contract No. DE-AC03-76SF00098), the National Energy Research Scientific Computing Center, and the International Centre for Diffraction Data. Research at the Advanced Light Source beamline 7.0, Lawrence Berkeley National Laboratory, was supported by the Department of Energy, Materials Sciences Division (Grant No. DE-FG02-92ER45468).

---

*Present address: Advanced Light Source, Lawrence Berkeley National Laboratory, University of California, Berkeley CA 94720.

[1] D. Gabor, Nature (London) **161**, 777 (1948).

[2] A. Szöke, in *Short Wavelength Coherent Radiation: Generation and Applications*, AIP Conf. Proc. No. 147, edited by T. Attwood and J. Boker (AIP, New York, 1986), p. 361.

[3] (a) J. J. Barton, Phys. Rev. Lett. **61**, 1356 (1988); **67**, 3106 (1991); (b) J. J. Barton and L. J. Terminello (unpublished); *Structure of Surfaces III*, edited by S. Y. Tong, M. A. Van Hove, X. Xide, and K. Takanayagi (Springer-Verlag, Berlin, 1991), p. 107; (c) S. Y. Tong, H. Huang, and C. M. Wei, Phys. Rev. B **46**, 2452 (1992), and references therein; (d) L. Fonda, Phys. Status Solidi B **188**, 599 (1995).

[4] B. P. Tonner, Z.-L. Han, G. R. Harp, and D. K. Saldin, Phys. Rev. B **43**, 14 423 (1991); D. K. Saldin, K. Reuter, P. L. De Andres, H. Wedler, X. Chen, J. B. Pendry, and K. Heinz, *ibid.* **54**, 8172 (1996).

[5] S. Thevuthasan, R. X. Ynzunza, E. D. Tober, C. S. Fadley, A. P. Kaduwela, and M. A. Van Hove, Phys. Rev. Lett. **70**, 595 (1993).

[6] (a) S. Y. Tong, H. Li, and H. Huang, Phys. Rev. B **51**, 1850 (1995); (b) H. Wu and G. J. Lapeyre, *ibid.* **51**, 14 549 (1995); (c) J. M. Roesler, M. T. Sieger, and T.-C. Chiang, Surf. Sci. **329**, L588 (1995); (d) M. T. Sieger, J. M. Roesler, D. S. Lin, T. Miller, and T.-C. Chiang, Phys. Rev. Lett. **73**, 3117 (1994).

[7] P. J. Rous and M. H. Rubin, Surf. Sci. **316**, L1068 (1994).

[8] (a) P. Hofmann, K.-M. Schindler, V. Fritzsche, S. Bao, A. M. Bradshaw, and D. P. Woodruff, J. Vac. Sci. Technol. A **12**, 2045 (1994); Surf. Sci. **337**, 169 (1995), and references therein; (b) D. P. Woodruff, R. Davis, N. A. Booth, A. M. Bradshaw, C. J. Hirschmugl, K.-M. Schindler, O. Schaff, V. Fernandez, A. Theobald, P. Hofmann, and V. Fritzsche, *ibid.* **357-358**, 19 (1996), and references therein.

[9] (a) L. J. Terminello, B. L. Petersen, and J. J. Barton, J. Electron Spectrosc. Relat. Phenom. **75**, 229 (1995), and references therein; (b) H. Wu, G. J. Lapeyre, H. Huang, and S. Y. Tong, Phys. Rev. Lett. **71**, 251 (1993), and references therein; (c) M. Zharnikov, M. Weinelt, P. Zebisch, M. Stichler, and H.-P. Steinrück, Thin Solid Films **275**, 266 (1996), and references therein; (d) R. Denecke, R. Eckstein, L. Ley, A. E. Bocquet, J. D. Riley, and R. C. G. Leckey, Surf. Sci. **331-333**, 1085 (1995); (e) J. G. Tobin, G. D. Waddill, H. Li, and S. Y. Tong, *ibid.* **334**, 263 (1995), and references therein.

[10] H. Li, S. Y. Tong, D. Naumovic, A. Stuck, and J. Osterwalder, Phys. Rev. B **47**, 10 036 (1993); D. K. Saldin, G. R. Harp, and X. Chen, *ibid.* **48**, 8234 (1993), and references therein.

[11] (a) Z.-L. Han, S. Hardcastle, G. R. Harp, H. Li, X.-D. Wang, J. Zhang, and B. P. Tonner, Surf. Sci. **258**, 313 (1991), and references therein; (b) I. H. Hong, S. C. Shyu, Y. C. Chou, and C. M. Wei, Phys. Rev. B **52**, 16 884 (1995), and references therein.

[12] (a) M. A. Mendez, C. Glück, J. Guerrero, P. L. De Andres, K. Heinz, D. K. Saldin, and J. B. Pendry, Phys. Rev. B **45**, 9402 (1992), and references therein; (b) C. M. Wei, S. Y. Tong, H. Wedler, M. A. Mendez, and K. Heinz, Phys. Rev. Lett. **72**, 2434 (1994), and references therein.

[13] S. Y. Tong, H. Huang, and X. Q. Guo, Phys. Rev. Lett. **69**, 3654 (1992).

[14] M. Tegze and G. Faigel, Europhys. Lett. **16**, 41 (1991); Nature (London) **380**, 49 (1996).

[15] (a) T. Gog, P. M. Len, G. Materlik, D. Bahr, C. Sanchez-Hanke, and C. S. Fadley, Phys. Rev. Lett. **76**, 3132 (1996); (b) T. Gog, R.-H. Menke, F. Arfelli, P. M. Len, C. S. Fadley, and G. Materlik, Synch. Rad. News **9**, 30 (1996); (c) P. M. Len, T. Gog, G. Materlik, and C. S. Fadley, Phys. Rev. B **55**, R3323 (1997); (d) P. M. Len, T. Gog, D. Novikov, R. A. Eisenhower, G. Materlik, and C. S. Fadley, *ibid.* **56**, 1529 (1997).

[16] D. K. Saldin, G. R. Harp, B. L. Chen, and B. P. Tonner, Phys. Rev. B **44**, 2480 (1991).

[17] S. Thevuthasan, G. S. Herman, A. P. Kaduwela, T. T. Tran, Y. J. Kim, R. S. Saiki, C. S. Fadley, and M. A. Van Hove, J. Vac. Sci. Technol. A **10**, 2261 (1992).

[18] P. Hu and D. A. King, Phys. Rev. B **46**, 13 615 (1992).

[19] P. M. Len, S. Thevuthasan, C. S. Fadley, A. P. Kaduwela, and M. A. Van Hove, Phys. Rev. B **50**, 11 275 (1994).

[20] P. M. Len, F. Zhang, S. Thevuthasan, A. P. Kaduwela, M. A. Van Hove, and C. S. Fadley, J. Electron Spectrosc. Relat. Phenom. **76**, 351 (1995); **85**, 145 (1997).

[21] (a) J. C. Buchholz, G. C. Wang, and M. G. Lagally, Surf. Sci. **49**,

508 (1975); (b) M. A. Van Hove and S. Y. Tong, Phys. Rev. Lett. **35**, 1092 (1975); (c) M. Arnold, S. Sologub, G. Hupfauer, P. Bayer, W. Frie, L. Hammer, and K. Heinz, Surf. Rev. Lett. **4**, 1291 (1997); (d) B. Kim, J. Chen, J. L. Erskine, W. N. Mei, and C. M. Wei, Phys. Rev. B **48**, 4735 (1993); (e) Y. Jugnet, N. S. Prakash, L. Porte, T. M. Duc, T. T. A. Nguyen, R. Cinti, H. C. Poon, and G. Grenet, *ibid.* **37**, 8066 (1998); (f) R. X. Ynzunza, Ph.D. dissertation, University of California at Davis, 1998.

[22] P. M. Len, C. S. Fadley, and G. Materlik, *X-ray and Inner Shell Processes: 17th International Conference*, AIP Conf. Proc. No. 389, edited by R. L. Johnson, H. Schmidt-Boeckering, and B. F. Sonntag (AIP, New York, 1997), p. 295.

[23] G. R. Harp, D. K. Saldin, X. Chen, Z.-L. Han, and B. P. Tonner, J. Electron Spectrosc. Relat. Phenom. **57**, 331 (1991).

[24] P. M. Len, S. Thevuthasan, A. P. Kaduwela, M. A. Van Hove, and C. S. Fadley, Surf. Sci. **365**, 535 (1996).

[25] R. X. Ynzunza (private communication).

[26] J. J. Rehr and R. C. Albers, Phys. Rev. B **41**, 8139 (1990).

[27] A. P. Kaduwela, D. J. Friedman, and C. S. Fadley, J. Electron Spectrosc. Relat. Phenom. **57**, 223 (1991).

[28] (a) SCAT photoelectron diffraction program package, Y. Chen, H. Wu, and D. A. Shirley (private communication); (b) MSCD photoelectron diffraction program package, Y. Chen, F. J. Garcia De Abajo, A. Chasse, R. X. Ynzunza, A. P. Kaduwela, M. A. Van Hove, and C. S. Fadley, Phys. Rev. B **58**, 13 121 (1998), http://electron lbl.gov/mscdpack/mscdpack.html.

[29] T. Greber, J. Osterwalder, D. Naumovic, A. Stuck, S. Hüfner, and L. Schlapbach, Phys. Rev. Lett. **69**, 1947 (1992); D. K. Saldin, G. R. Harp, and B. P. Tonner, Phys. Rev. B **45**, 9629 (1992); J. J. Barton and L. J. Terminello, *ibid.* **46**, 13 548 (1992).

[30] S. Tanuma, C. J. Powell, and D. R. Penn, Surf. Interface Anal. **11**, 577 (1988).

[31] *Surface Crystallography by LEED*, edited by M. A. Van Hove and S. Y. Tong (Springer-Verlag, New York, 1979).

[32] L. J. Terminello, J. J. Barton, and D. A. Lapiano-Smith, J. Vac. Sci. Technol. B **10**, 2088 (1992).

[33] S. D. Ruebush, R. X. Ynzunza, S. Thevuthasan, A. P. Kaduwela, M. A. Van Hove, and C. S. Fadley, Surf. Sci. **328**, 302 (1995).

[34] T. Greber and J. Osterwalder, Chem. Phys. Lett. **256**, 653 (1996); (private communication).

[35] M. T. Sieger (private communication).